Jour. of the KGS, Vol. 22, No. 9. September 2006, pp. 23~36

Assessment of Ultimate Bearing Capacity for an Embedded Wall by Closed-Form Analytical Solution

근사적인 해석법에 의한 근입된 벽체의 극한지지력 평가

Lee, Yong-Joo[1] 이 용 주

요 지

본 연구는 사질토 지반에 근입되어 있는 벽체의 극한지지력을 구하기 위해 새로운 근사적인 해석법의 전개과정에 대해 설명한다. 이러한 근사적인 형태의 해석기법은 상계 및 하계법으로 구성되어 있다. 상·하계법으로 계산된 값은 소성영역에서 구해진 2차원 실내벽체모형의 하중재하시험 및 유한요소해석 결과와 비교하였다. 비교 결과, 모형실험과 유한요소해석으로부터 구한 극한하중 값은 상계와 하계 사이에 모두 분포하는 것으로 나타났다. 이러한 비교에서 특이 할 사항은 하계법으로 구한 벽체의 극한하중이 모형실험 및 유한요소해석에서 구한 극한하중과 잘 일치되는 것을 보여 주었다. 그러나, 평면변형률 조건에서 기존의 경험적인 식에 의한 계산에서 얻어진 극한하중은 하계법의 극한하중에 훨씬 못 미치는 것으로 나타났다.

Abstract

This study presents the development of a new closed-form analytical solution for the ultimate bearing capacity of an embedded wall in a granular mass. The closed-form analytical solution consists of upper and lower bound solutions (UB and LB). The calculated values from these bound solutions were compared with the author's two-dimensional laboratory wall model loading test and finite element analysis in the plastic region. The comparison showed that ultimate bearing loads from both the model test and finite element analysis are located between UB and LB. In particular, the ultimate bearing load from LB showed good agreement with the ultimate bearing load values from both the model test and finite element analysis. However, the calculated value from the conventional empirical form subjected to plane-strain conditions was shown to be much smaller than the LB.

Keywords : Closed-form analytical solution, Embedded wall, Finite element analysis, Model wall loading test, UB and LB, Ultimate bearing capacity

1. Introduction

Piles are a long established technique dominated by practice rather than advanced current research. Load capacities are still at times in doubt, and in important projects, pile load testing is therefore still commonly adopted as the method of checking the performance of a pile (P-S behaviour).

In deep piles, the end-bearing capacity is less clear than the values derived for shallow foundations. For drained conditions ($\phi'>0$), Terzaghi's (1943) end-bearing type failure pattern of a two-dimensional strip footing consists of three distinct zones, viz. "active zone" directly under the footing (triangular wedge), "fan zone" next the active

1 Member, Senior Researcher, Steel Structure Research Laboratory, Research Institute of Industrial Science & Technology (RIST), ucesyjl99@rist.re.kr

zone (defined as a lo-spiral), and "passive zone" next the fan zone. However, in calculation of pile's bearing capacity, the side friction component should be included. The failure mechanism proposed by Meyerhof (1951) matches the stress discontinuity pattern which is used for a localised lower bound calculation but is not kinematically admissible for an upper bound mechanism. A modification of Meyerhof's (1951) mechanism appears to fit the author's shear strain data from both the model pile load test and the finite element analysis.

The basic concepts of carrying out upper and lower bound solutions are presented by Chen (1975), Atkinson (1981) and Powrie (1997). These concepts were applied in this study. Recently, some researchers have studied geotechnical problems with these bound solutions, particularly for non-associative flow rule (Drescher and Detournay, 1993; Davis and Selvadurai, 2002).

In this study, a row of loaded piles embedded in a granular mass was assumed to be an embedded wall which satisfies the two-dimensional plane-strain conditions rather than three-dimensional conditions.

2. Basic Bound Solution Concepts for ϕ' Soil

2.1 Introduction

One of the procedures for developing the possible failure mechanism of bearing pressure problem is to consider the stress discontinuities adopted for a lower bound approach and to couple these with the slip characteristic directions between the stress discontinuity zones. This is shown as a simple case in Fig. 1. The case is an undrained bearing capacity in C_u material. The single discontinuity XZ and the two slip characteristics α and β are shown in Fig. 1 (b) with their corresponding Mohr's circles for stress in Fig. 1 (a). The resulting mechanism is obtained by choosing critical slip lines PQ and QR, as shown in Fig. 1 (c) giving two blocks A and B in which a virtual work calculation provided an upper bound solution. If the best lower and upper bound solution are correspond and provide an identical answer, this solution is acceptable as satisfying both equilibrium and kinematically compatibility and does not violate failure criterion.

2.2 Lower Bound

The conceptual idea for lower bound solution is that, in a critical point of the problem, all material has just reached its failure value for the undrained case illustrated in Fig. 1 where the unique strength C_u is applied. For the author's tests on a granular mass, the control is in the critical state friction angle, ϕ'_{cs} shown by the limiting stress envelope in Fig. 2 (a). A stress discontinuity will separate two stress states with one common plane across which equilibrium is maintained resulting in a common stress state point C, as shown in Fig. 2 (b). ρ' is defined as the angle of mobilised friction on this common plane or discontinuity. Also, the change in principal stress direction across the discontinuity is θ_B-θ_A=$\delta\theta$, as shown in Fig. 2 (b).

In Fig. 2 (c), the line ρ' cuts circle O_A at C_1 and circle O_B at C_2 by geometry. O_B-C_2 is parallel to O_A-C_1, therefore $\angle XO_BC_2$ is equal to $2\theta_A$ (i.e. $\angle O_BO_AC_1$). As

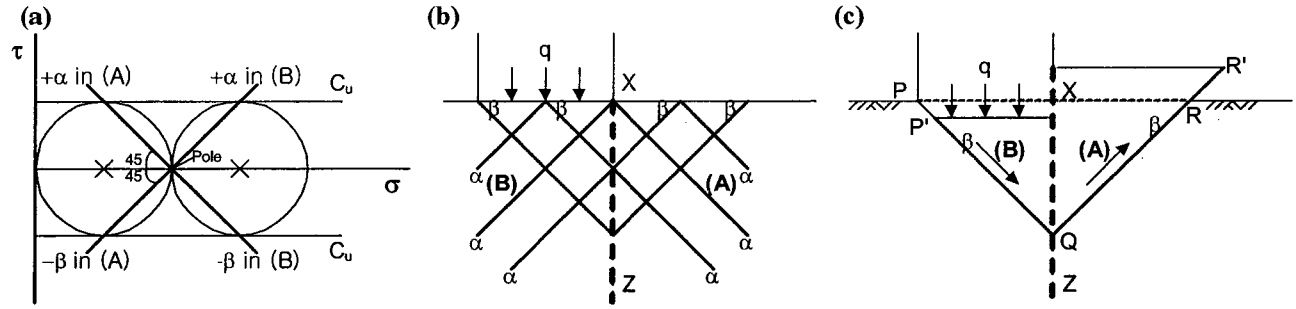

Fig. 1. Possible failure mechanism associated with rupture lines in C_u material: (a) Mohr circles with a pole point; (b) α and β characteristic lines; (c) Possible mechanism

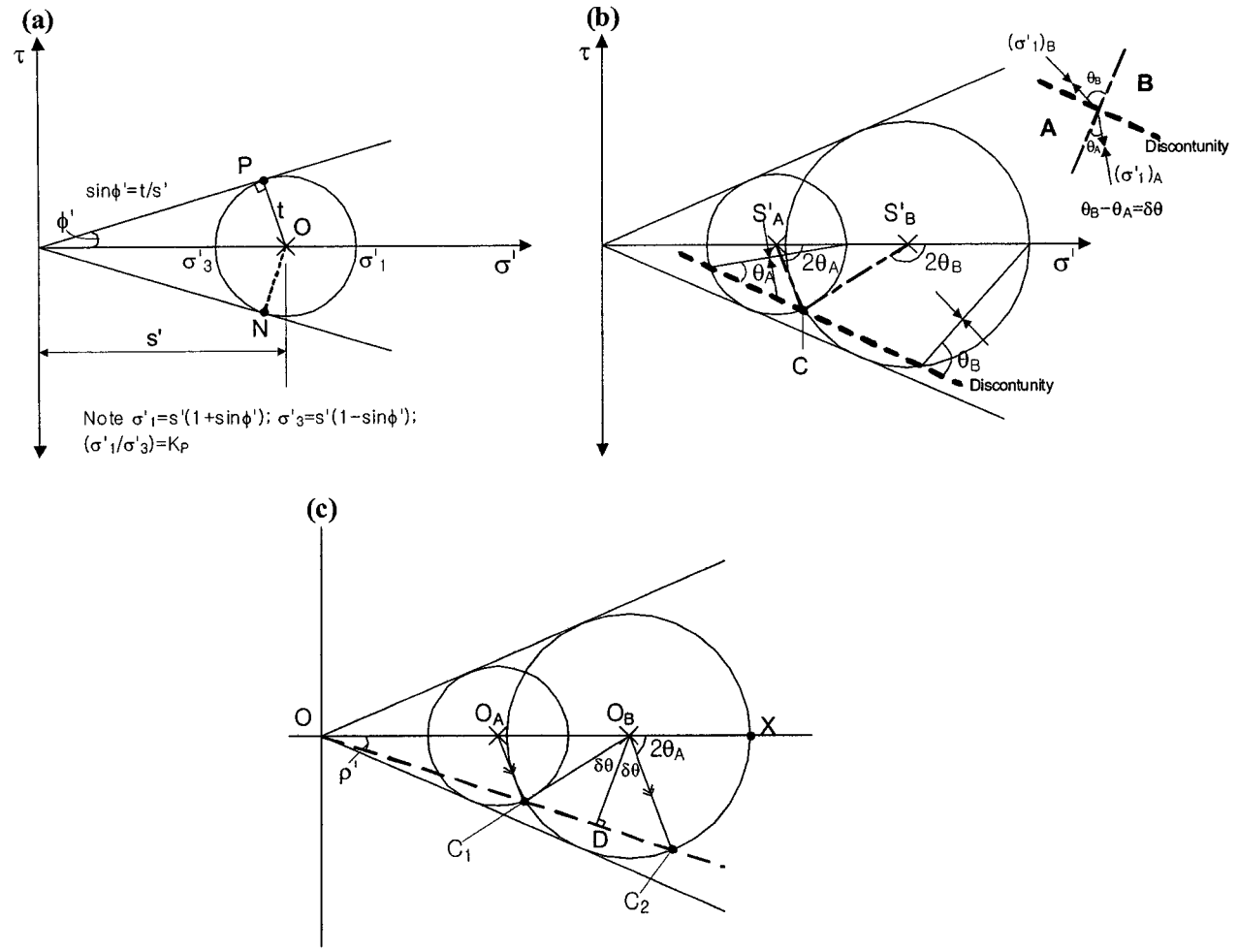

Fig. 2. (a) Mohr's circle for stress with a limiting envelope for ϕ' material; (b) Two stress states with discontinuity and a common point ; (c) Relationship between ρ' and $\delta\theta$ in two Mohr's circles

$\angle XO_BC_1$ is $2\theta_B$ then $\theta C_1O_BC_2=2\theta_A-2\theta_B=2\delta\theta$. If O_BD is set at 90° to OC_1C_2 then $\angle C_1O_BD=\angle C_2O_BD=dq$. O_BD can be expressed in terms of S'_B and ρ' and of t_B and $\delta\theta$:

$$O_BD = S'_B \sin\rho' = t_B \cos\delta\theta \tag{1}$$

Thus, ρ' can be determined as below:

$$\sin\rho' = \sin\phi' \cos\delta\theta \tag{2}$$

From the angles $\angle O_BC_2C_1$ (i.e. $\angle P=90°-\delta\theta$) and ρ' as shown in Fig. 3 (a), they give $\angle O_B0_AC_1=P+\rho'$ and $\angle O_AO_BC_1=P-\rho'$. Therefore, $2\theta_A=P+\rho'=90°+\rho'-\delta\theta$ and $2\theta_B=180°-(P-\rho')=90°+\rho'+\delta\theta$. These angles ($\theta_A$ and θ_B) can be rewritten as below:

$$\theta_A = (45° + \frac{\rho'}{2}) - \frac{\delta\theta}{2} \tag{3}$$

$$\theta_B = (45° + \frac{\rho'}{2}) + \frac{\delta\theta}{2} \tag{4}$$

The geometry associated with both angles θ_A and θ_B are shown in Fig. 3 (b). The distance between O_A and O_B represents the change in S'_A to S'_B, as shown in Fig. 3 (c). The stress ratios, i.e. t_B/t_A and S'_B/S'_A can be expressed as below:

$$\frac{t_B}{t_A} = \frac{\sin(P+\rho')}{\sin(P-\rho')} = \frac{S'_B}{S'_A} \tag{5}$$

as $P=90°-\delta\theta$, the above Eq. (5) can be written as below:

$$\frac{S'_B}{S'_A} = \frac{\cos(\delta\theta-\rho')}{\cos(\delta\theta+\rho')} \tag{6}$$

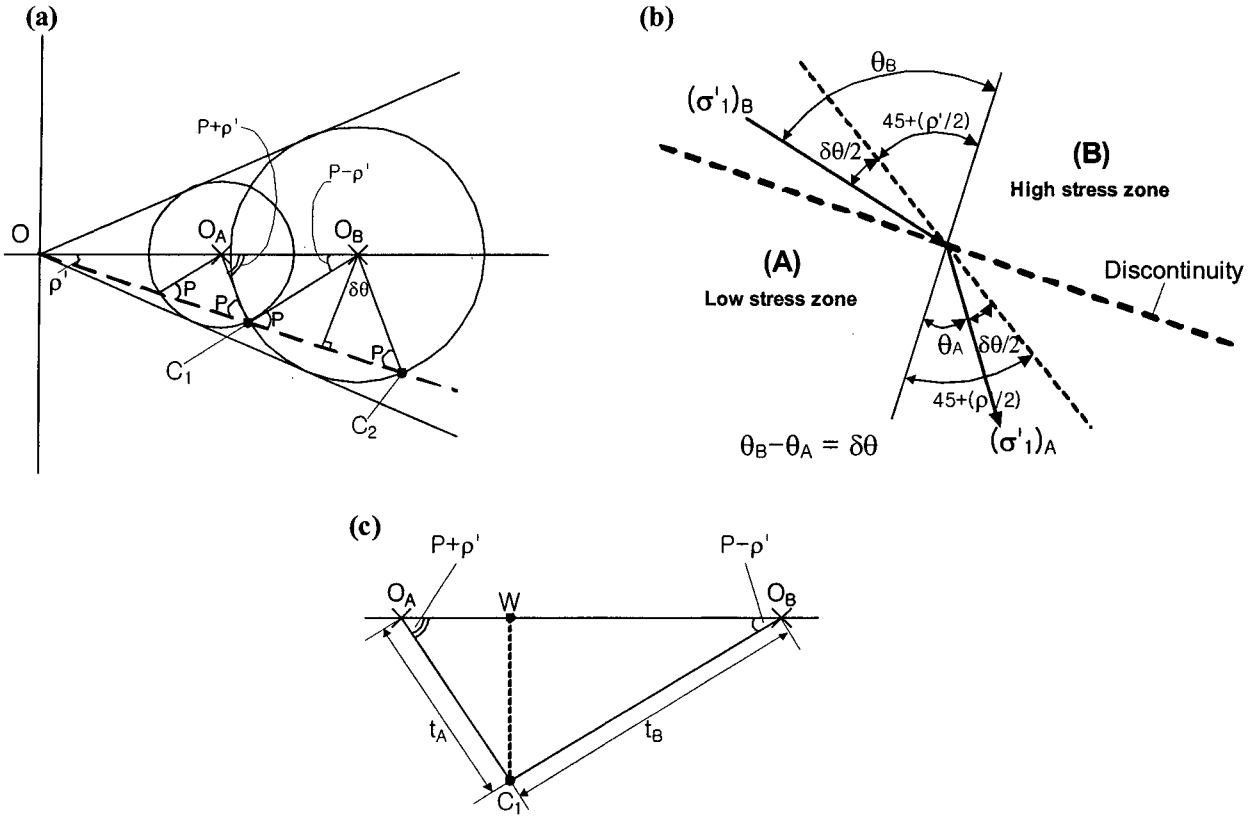

Fig. 3. (a) Calculation of θ_A and θ_B based on ρ' and $\delta\theta$; (b) Discontinuity with σ'_1 directions; (c) Geometry of S'_A and S'_B with t_A and t_B

if S'_B-S'_A=ΔS (where S'= S'_A), then

$$(S'+\Delta S')\cos(\delta\theta+\rho') = S'\cos(\delta\theta-\rho')$$

$$\Delta S'\cos(\delta\theta+\rho') = S'\cos(\delta\theta-\rho') - S'\cos(\delta\theta+\rho')$$

$$\Delta S'\cos(\delta\theta+\rho') = S'[(\cos\delta\theta\cos\rho' + \sin\delta\theta\sin\rho') - (\cos\delta\theta\cos\rho' - \sin\delta\theta\sin\rho')]$$

$$\frac{\Delta S'}{S'}\cos(\delta\theta+\rho') = 2\sin\delta\theta\sin\rho'$$

Therefore, we can obtain Eq. (7) as below:

$$2\sin\delta\theta\sin\rho' = \frac{\Delta S'}{S'}\{\cos\delta\theta\cos\rho' - \sin\delta\theta\sin\rho'\} \quad (7)$$

For very small changes in $\delta\theta$ across a discontinuity such as $\delta\theta \rightarrow 0$; $\cos\delta\theta \rightarrow 1$; $\sin\delta\theta \rightarrow d\theta$; $2\sin\delta\theta \rightarrow 2d\theta$; $\rho' \rightarrow \phi'$, the above Eq. (7) can be rewritten as below:

$$2d\theta\tan\phi' = \frac{dS'}{S'} \quad (8)$$

For a whole sequence of small angle changes the discontinuities will form a fan. This will change the principal stress direction, $\Delta\theta$ provided:

$$2\tan\phi'\int_0^{\Delta\theta} d\theta = \int_{S'_A}^{S'_B}\frac{1}{S'}dS' \quad (9)$$

giving Eq. 10 below:

$$\exp^{2\Delta\theta\tan\phi'} = \frac{S'_B}{S'_A} \quad (10)$$

In order to draw acceptable fields based on straight lines rather than the log spiral, the author chose to generate stress characteristic lines (α and β), based on a $\delta\theta$ of 15° and for a ϕ' of 26°. These were chosen to provide simple whole angles when using $\delta\theta/2$ and $\rho'/2$. The reason will be clear by Table 1 below. The mobilised friction angle (ρ') and the angles of major principal stress (σ_1) direction (θ_A and θ_B) were calculated, giving the

Table 1. Parameters for stress characteristic lines

ϕ'	ρ'	θ_A	θ_B
26°	25°	50°	65°

Note: $\delta\theta=\theta_B-\theta_A$=15° (angle change of σ'_1 direction in the stress field)

values of ρ', θ_A and θ_B as shown and the stress ratio change S'_B/S'_A=1.3.

Both α (positive) and β (negative) stress discontinuity planes for a succession of zones are shown in Fig. 4 (a). The β stress discontinuity (between E and F) cuts Mohr circles E and F at point C, as shown in Fig. 4 (b).

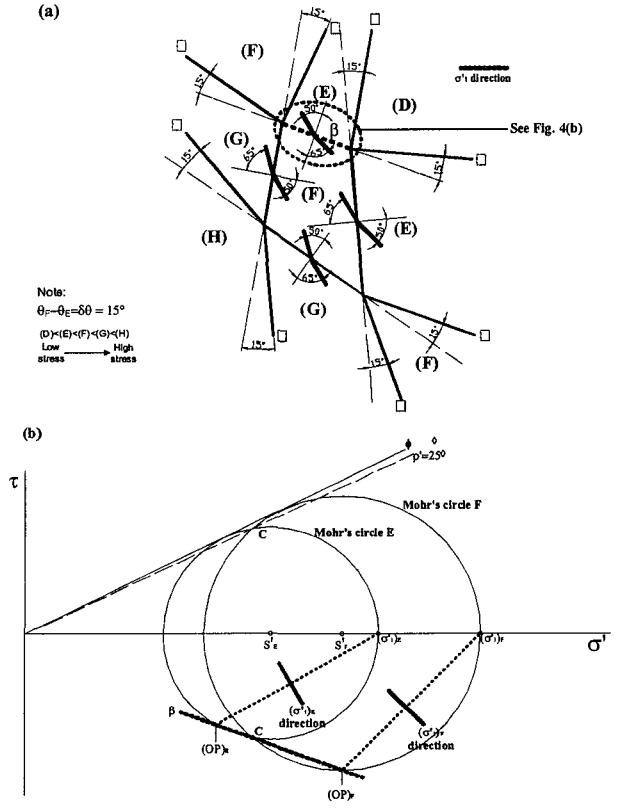

Fig. 4. (a) Stress characteristic lines with $\delta\theta$=15°; (b) Mohr circles with stress discontinuity (β) for E and F

2.3 Upper Bound

To obtain the upper bound solution in this study, four key assumptions are summarised as below:

(1) The soil is permeable and drains. The water is therefore not involved in any displacements. In the author's case, the whole experiment is dry.

(2) The granular soil dilates at failure on the obliquity (ϕ' or ρ') planes, as shown in Fig. 5 (a). The corner of the element moves from the point a to a' as the shear occurs rising to the angle of dilation (Ψ). To maintain coincidence of principal axes (i.e. σ_1 and ε_1 directions are the same), normality is assumed for the material behaviour resulting in the angle of Ψ being equal to ϕ', as shown in Fig. 5 (b). This assumption is known to be incorrect for granular material. No soil has ever known to dilate at more than 26° whereas ϕ' is usually much greater than 30°. However, in an upper bound approach any assumption made will only influence the accuracy. It is known that if the mechanism chosen is closely associated with the best stress field, the error will be minimised. The author's assumption of $\delta\theta$=15° and the approach above provides an acceptable upper bound.

(3) Upper bounds involve an assessment of internal work for the virtual work calculation. This involves work

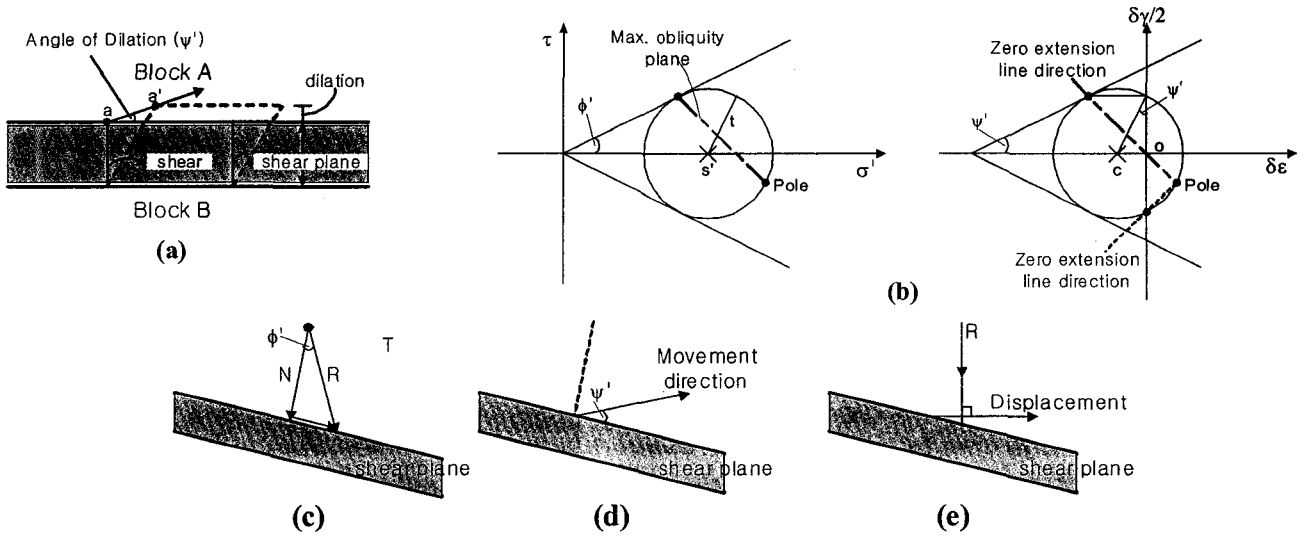

Fig. 5. ϕ' material for the upper bound: (a) Rupture system; (b) Mohr's circles related to maximum obliquity planes; (c) Relation between N and T; (d) Movement direction with Ψ; (e) Relation between R and displacement

done on the shear planes. The relationship between the normal force (N) and shear force (T) is associated by ϕ' giving a resultant force (R), as shown in Fig. 5 (c). The dilation (y) away from the line of the shear plane means the movement shown in Fig. 5 (d). If $\Psi=\phi'$ then the resulting force, R and the displacement are at right angles to each other, as shown in Fig. 5 (e). Hence, no internal work is done by R. This means that no internal work is done on failure or shear planes. This is obviously an extreme situation, but the result is, of course, considerable displacements of the external forces which form the remaining component of the virtual work balance. The large movement of the displaced resulting forces compensates the elimination of internal work.

(4) In relation to the rupture fan mechanism, the ruptures are formed of two sets governed by the zero extension line directions shown in Fig. 6 (a). These are separated by the angle of $90°+\Psi$. The rupture plane o-a-b-n is a smooth curve through the fan field for a small angle change (i.e. $\delta\theta$) in the fan. The α rupture will curve through the same angle. As the plane a-b must be at $90°+\Psi$ to the radius b-P, for a small angle of $\delta\theta$ the radius P-b becomes $R+\delta R$ and the length a-x is $Rd\theta$. Therefore,

$$\frac{dR}{Rd\theta}=\tan\psi \quad \text{or} \quad \frac{dR}{R}=\tan\psi d\theta \tag{11}$$

and then integrating the above Eq. 11:

$$\log_e[R]_{R_A}^{R_B}=[\theta\tan\psi] \tag{12}$$

The radius changes can be expressed as

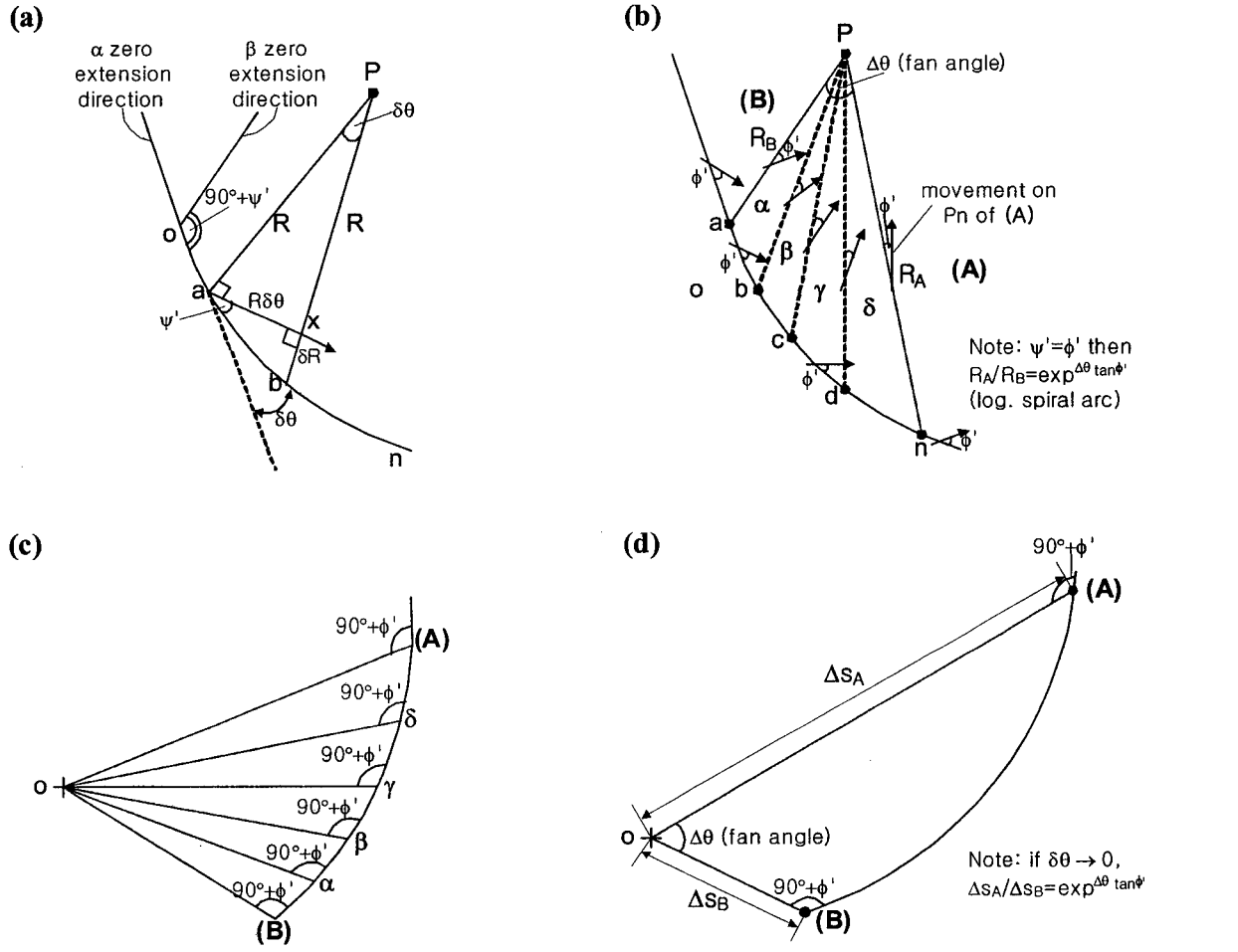

Fig. 6. ϕ' material for the upper bound: (a) Zero extension line directions; (b) Logarithmic spiral fan system; (c) Displacement diagram for a log spiral fan mechanism; (d) Identical displacement diagram of log spiral

$$\frac{R_B}{R_A} = \exp^{\theta_{BA} \tan\psi} \tag{13}$$

If Ψ is equal to ϕ', the equation of a log spiral can be expressed as below:

$$\frac{R_B}{R_A} = \exp^{\Delta\theta \tan\phi'} \tag{14}$$

If Ψ is equal to 0 (i.e. no dilation, no volume change, undrained conditions), the radius ratio, $R_B/R_A=1$. This means that the shape is a circle as shown in Fig. 6 (a). Fig. 6 (c) shows the displacement diagram associated with the physical failure fan in relation to Fig. 6 (b). If $\delta\theta$ is very small (i.e. $\delta\theta \rightarrow 0$), the displacement diagram will be an identical type of log spiral, as shown in Fig. 6 (d).

2.4 Example of an Exact Solution for a Footing in ϕ' Soil

Fig. 7 shows the example of a footing problem in a granular mass. An exact solution (i.e. LB=UB) of the ultimate bearing load (q′) was successfully calculated:

$$q' = PK_P \exp^{2(\pi/2)\tan\phi'} \tag{15}$$

where K_P is the coefficient of passive earth pressure (see Fig. 2 (a)).

This is a simple case in which soil assumed as weightless soil. In this study, a deep wall case is more difficult to obtain the exact solution due to the side friction component around the wall and soil's self weight.

3. Laboratory Wall Model Loading Test

The author has conducted two-dimensional wall model loading test using a multiple sized aluminium rod mixture. The author's aluminium rod mixture contained six different diameters (viz. 2 mm, 3 mm, 6 mm, 9 mm, 12 mm and 20 mm): all are 75mm in length. It represented a well graded, idealised two-dimensional granular material (Lee, 2004). In the model test, DCM (displacement control method) using the screw jack was adopted to generate large pile displacements associated with failure mechanism, as shown in Fig. 8. More details of test procedures are summarised by Lee (2004). Displacement and strain data during the wall loading was obtained by means of close

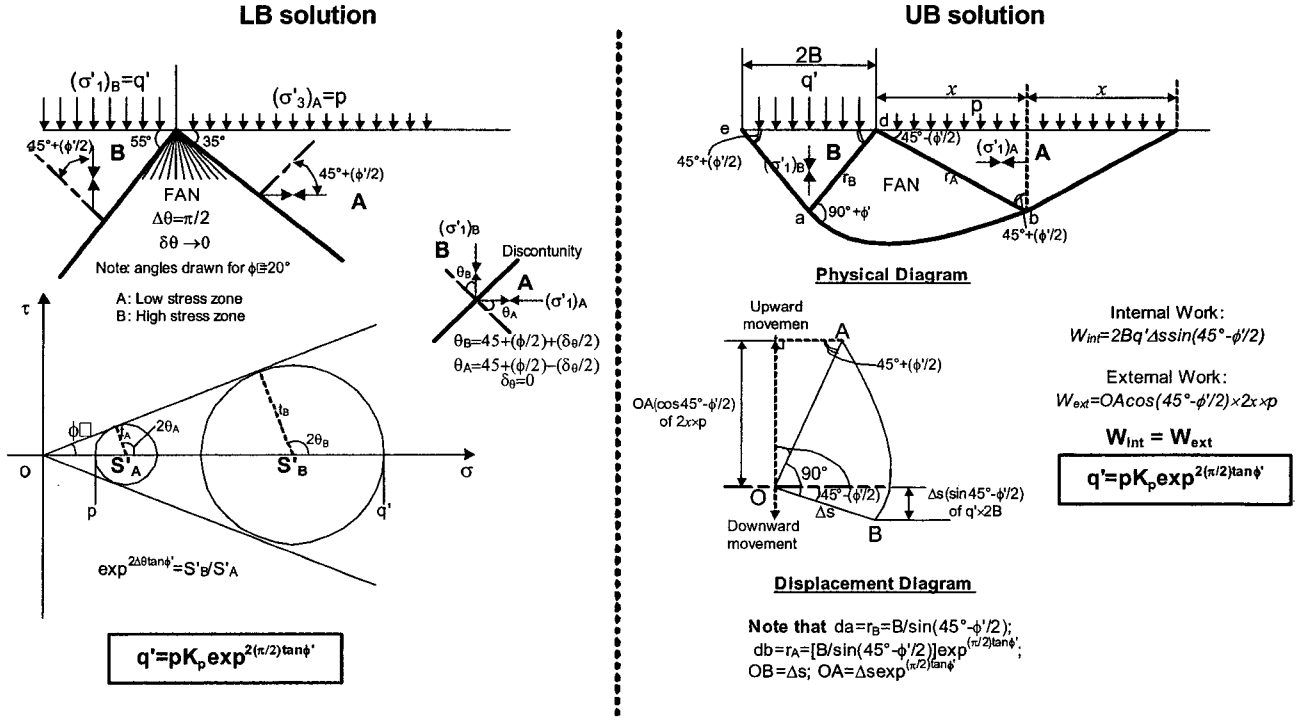

Fig. 7. An exact solution for the shallow footing on ϕ' material

range photogrammetric technique (Lee and Bassett, 2006). The displacement and strain data from the model test show good agreement with the finite element analysis (Lee, 2005a). Based on the displacement vectors from the model test and the maximum shear strain data from the finite element analysis, kinematically admissible failure mechanisms were proposed to develop the upper bound approach. These postulated mechanisms are shown in Fig. 9. It should be noted that more details of the finite element analysis such as boundary conditions, wall loading simulation and material properties are described by Lee (2005b).

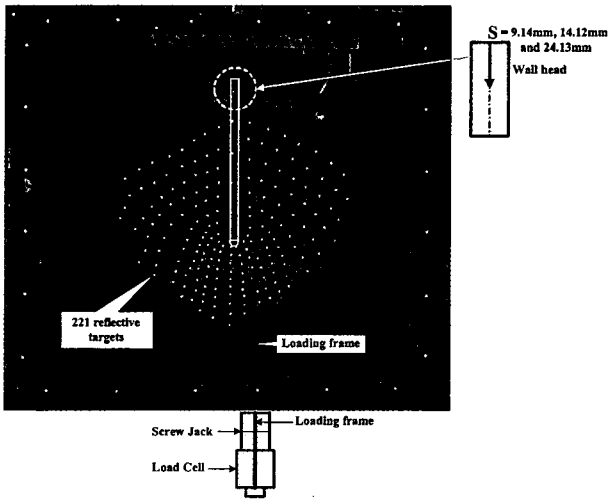

Fig. 8. Two-dimensional wall model loading test by DCM

4. Assessment of an Ultimate Wall Bearing Load

4.1 Lower Bound Approach

In Fig. 10, the author postulates a stress field for the wall with a side friction angle of 13°. This gives rise to a tip fan with an angle of $\Delta\theta$=68°. This case is referred to as case LB-01. The principal stress then rotates from zone B through 90° to element A, where the vertical stress due to self weight provides the σ'_3 value. To assess the wall side friction, the zone δ_{high} (σ'_1 direction in the high stress zone) is typical. And from this zone, the major principal stress direction rotates 22° to reach δ_{low} (σ'_1 direction in the low stress zone), i.e. 68° to 90°. The stress situation in the side friction zones is described by the Mohr circle of stress, as shown in Fig. 11.

As an alternative, the single stress fan, $\Delta\theta$=189° can be assumed. This is referred to as case LB-02 shown in Fig. 12. The stress situation in zone A against the side

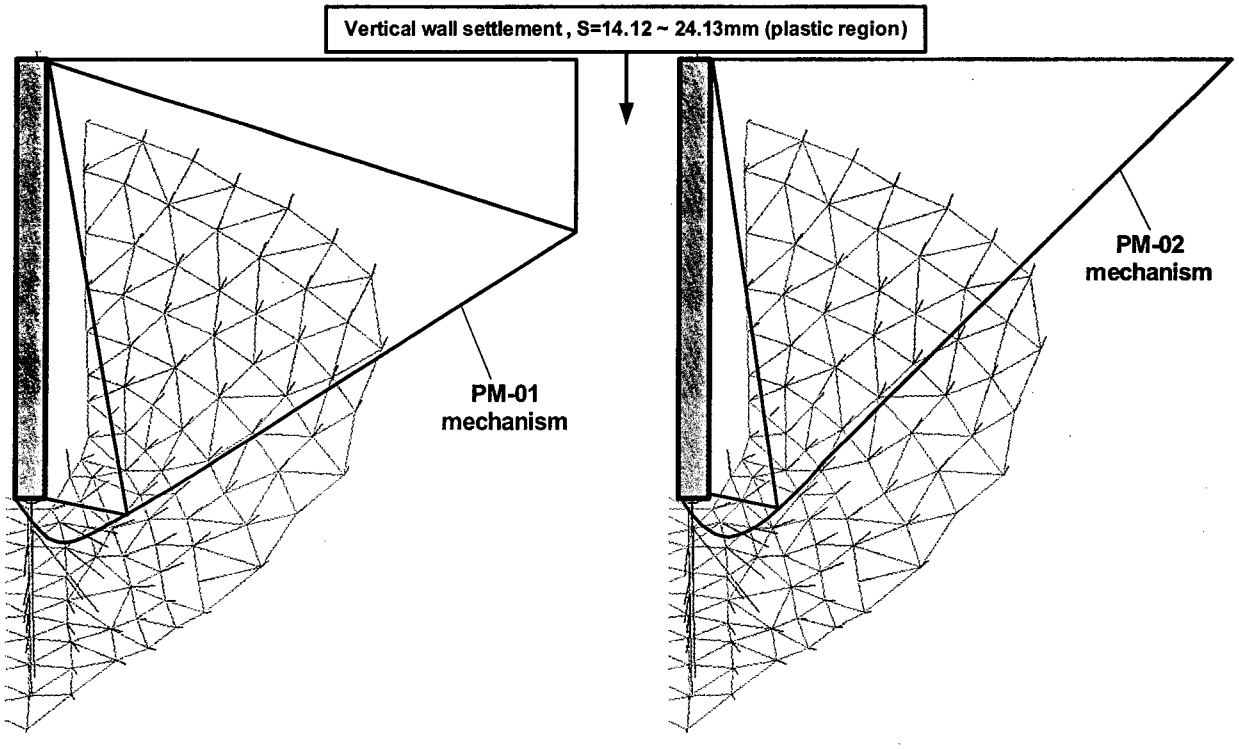

Fig. 9. Postulated failure mechanisms PM-01 and PM-02 (in the large shear strain propagation) based on displacement vectors from model test

of the wall is as described by the Mohr circle of stress, as shown in Fig. 13. This gives rise to a principal stress direction at 9° as shown. From zone B below the wall σ'_1 therefore rotates 189°. The author has drawn $\delta\theta$=15° zones from 0 to 180° and a single 9° zone to the side friction area B. The ultimate wall loads for both LB-01 and LB-02 were calculated (see Appendix) and will be described in the following Section 4.3.

4.2 Upper Bound Approach

At this stage, it is important at this stage to note that

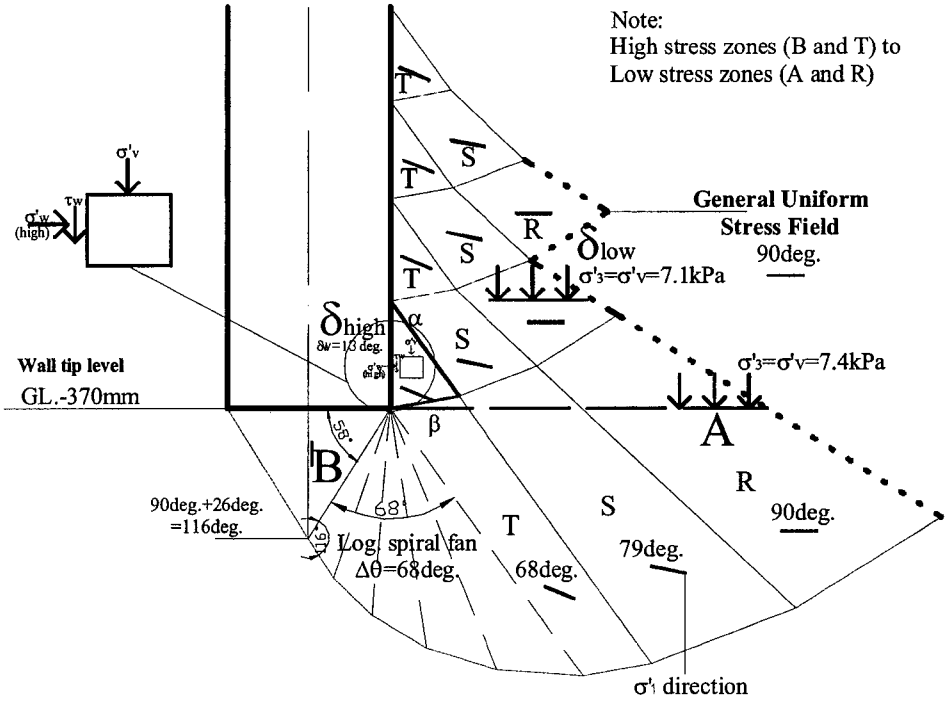

Fig. 10. Postulated stress field with log spiral fan of $\Delta\theta$=68° (LB-01)

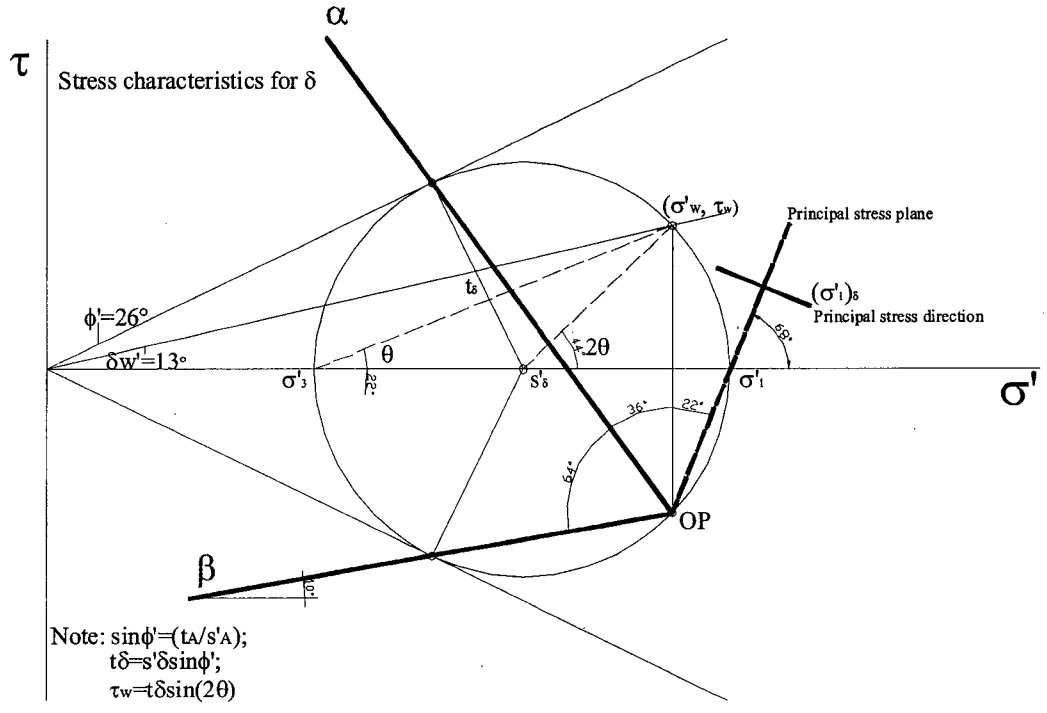

Fig. 11. Stress characteristic lines with Mohr's circle for stress in zone T (at the wall side) with δ_w side friction

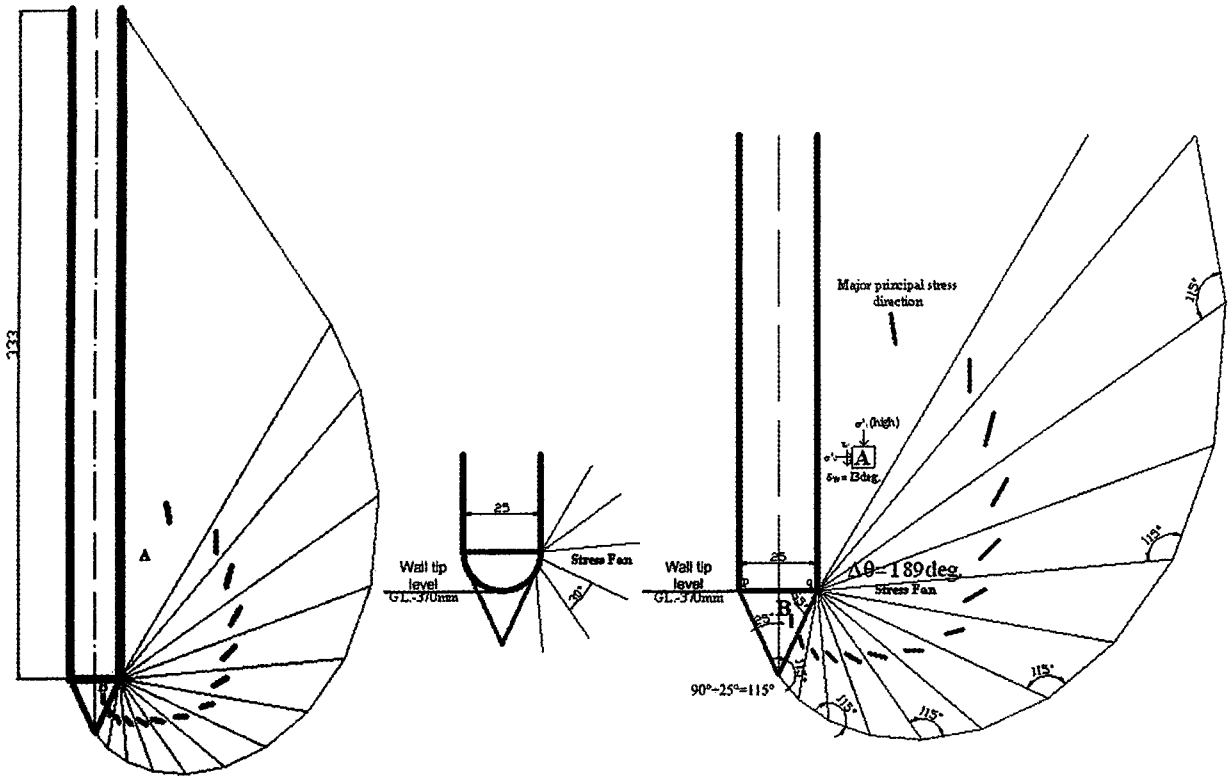

(a) (b)

Fig. 12. Stress fan with log spiral fan of $\Delta\theta$=189° (LB-02): (a) Postulated stress field with log spiral fan; (b) Stress situation in A

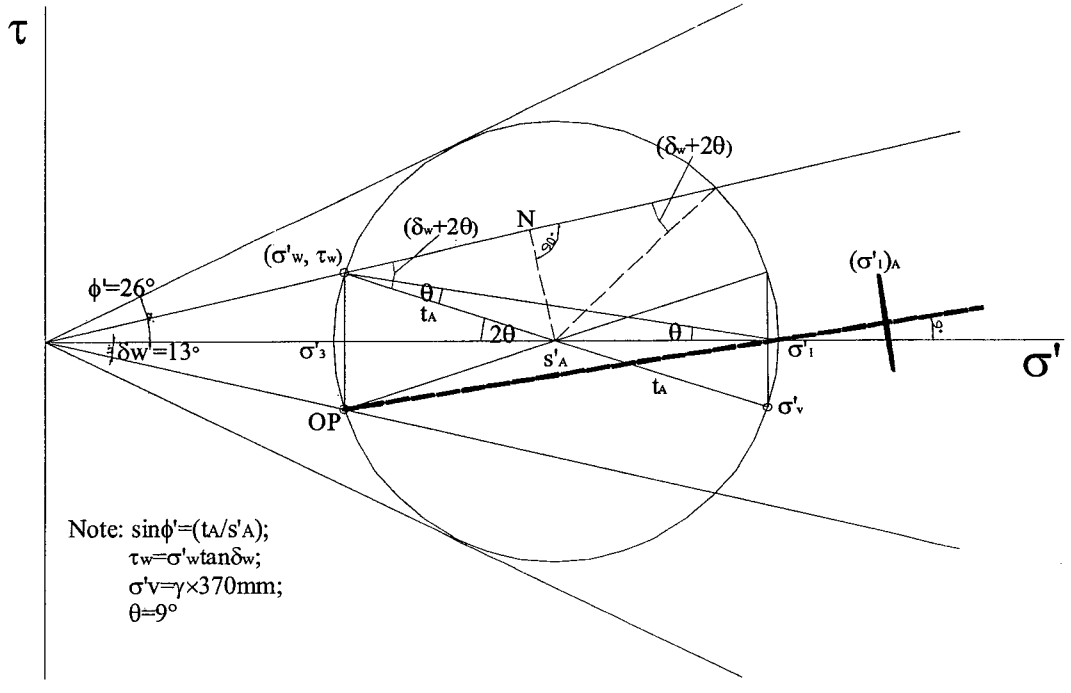

Fig. 13. Mohr's circle for stress in the low stress zone A (at the wall side)

a compatible kinematically admissible mechanism cannot be developed for the second case of the LB-02 proposal, as the resulting displacements for any angle of dilation have to move soil across the wall boundary. Therefore, the upper bounds discussed are associated with a small extension of LB-01.

As described in Fig. 9 two kinematically admissible failure mechanisms (viz. PM-01 and PM-02) have been

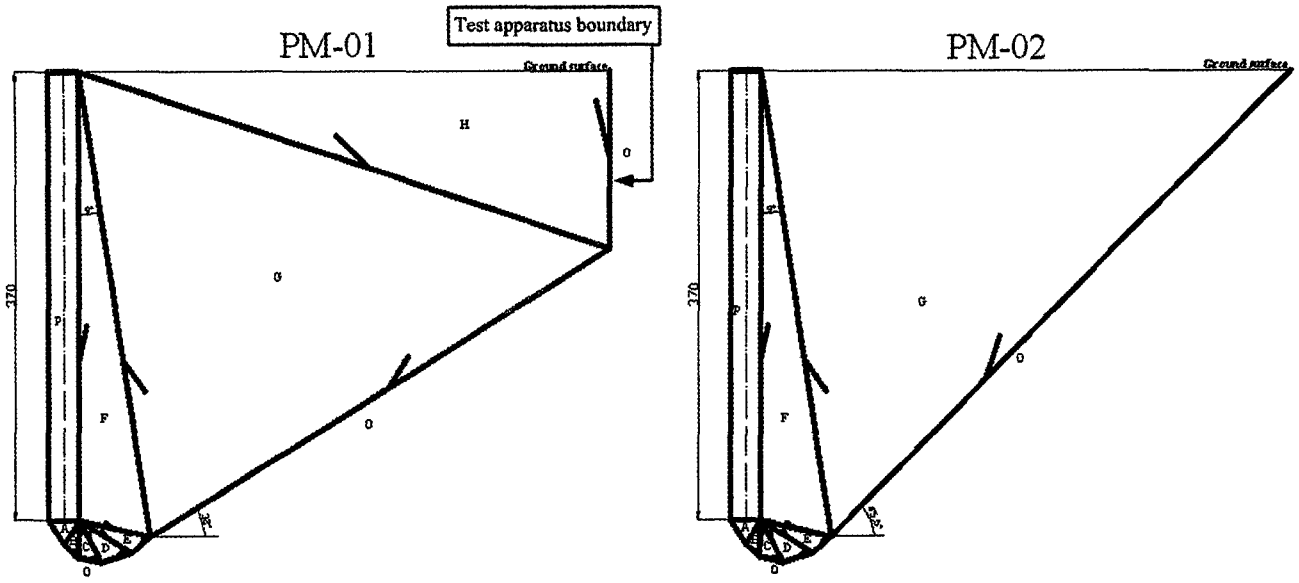

Fig. 14. Upper bound mechanisms PM-01 and PM-02 with displacement vectors

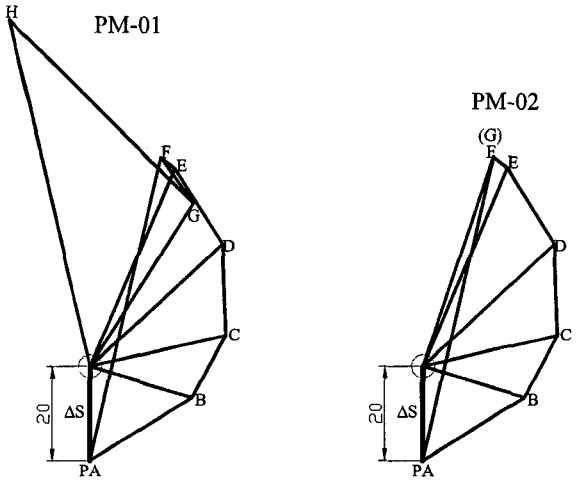

Fig. 15. Corresponding displacement diagrams for upper bound mechanisms PM-01 and PM-02

postulated, as shown in Fig. 14. It should be noted that these upper bound mechanisms basically started from zone A to F ($\delta\theta$=15° on each) with larger blocks F, G and H for PM-01, and F and G for PM-02 completing admissible upper bound mechanisms involving the wall side and apparatus boundaries. The corresponding displacement diagrams are shown in Fig. 15. The vertical downward movement of the wall tip was assumed as ΔS in the displacement diagrams. It can quickly be seen that, as weight is the fundamental stabilising force, the smallest upward vertical displacements and area G only are given by PM-02. The upper bound calculations for the upper bound mechanisms carried out are described in Section 4.3. It should be noted that the fully detailed upper bound calculation for PM-02 is represented in Appendix.

4.3 Plastic Failure Wall Load

The calculated ultimate wall loads for the lower and upper bounds were compared to the real failure wall load from the physical wall loading test and finite element analysis. These ultimate wall loads are summarised below in Table 2. It is noted that FEA value is based on the unit length of 1m and model test value is based on the wall length of 75 mm.

The upper bound solution from PM-02 was the lowest UB solution. The author believed that the true plastic failure wall load would be located between LB-01 and

Table 2. Ultimate wall loads (P_u)

Real value		LB		UB	
		LB-01	LB-02	PM-01	PM-02
FEA (unit length: 1 m)	4.6 kN	4.3 kN	4.98 kN	11.3 kN	8.4 kN
Model Test (unit length: 75 mm)	34.5 kg	32 kg	37.2 kg	84.3 kg	63 kg

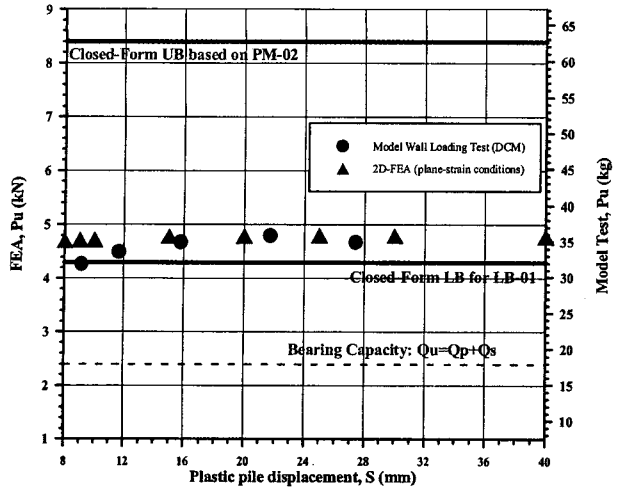

Fig. 16. Comparison of ultimate load (P_u) between bound solutions and model test with FE data

PM-02. The model test and FEA data in the plastic region between displacements of S=8 mm to 40 mm were compared to UB solution (PM-02) and LB solution (LB-01) with the conventional calculation (Tomlinson and Boorman, 1986), as shown in Fig. 16. The conventional calculation value considering end-bearing and side friction is shown in Appendix. The classical upper and lower bound solutions bracketed the real data lying close to the lower bound value. However, the value from the conventional empirical form subjected to plane-strain conditions is shown to be much smaller than the LB. The conventional calculation shown in this study is exclusively dependent on one material parameter ϕ' (internal friction angle) rather than N values from the field test result.

5. Conclusions

The assessment of the wall by upper and lower bound plastic failure analysis proved quite difficult, particularly regarding the influence of the side area of the deep wall. However, these classical approaches bracketed well the ultimate wall loads from both the model test and finite element analysis. In particular, the ultimate bearing load from the LB-01 showed good agreement with the ultimate bearing loads from both the model test and FEA. Through this study, the author believes that if the best upper bound mechanism (associated with satisfaction of displacement compatibility) can be sought, the UB solution may be close to the LB as well as real data.

References

1. Atkinson, J. H. (1981), *Foundations and Slopes*, McGraw-Hill, UK.
2. Chen, W. F. (1975), *Limit analysis and plasticity*, Development in Geotechnical Engineering, Vol.7, Elsvier.
3. Davis, R. O. and Selvadurai, A. P. S. (2002), *Plasticity and Geomechanics*, Cambridge University Press, UK.
4. Drescher, A. and Detournay, E. (1993), "Limit load in translational failure mechanisms for associative and non-associative materials", *Geotechnique*, Vol.43, No.3, pp.443-456.
5. Lee, Y. J. (2004), *Tunnelling adjacent to a row of loaded piles*, PhD Thesis, University College London, University of London.
6. Lee, Y. J. (2005a), "Laboratory model test of pile using photogrammetry", *Proceeding of the 2005 Annual Conference of KSCE*, October 20~21, 2005, Jeju, Korea, pp.3953-3956.
7. Lee, Y. J. (2005b), "P-S characteristics for end-bearing pile in granular material", *Jour. of the KGS*, Vol.21, No.2, pp.85-91.
8. Lee, Y. J. and Bassett, R. H. (2006), "Application of photogrammetric technique to a model tunnel", *Tunnelling and Underground Space Technology*, Vol.21, No.1, pp.79-96.
9. Meyerhof, G. G. (1951), "Ultimate bearing capacity of foundations", *Geotechnique*, Vol.2, No.4, pp.301-332.
10. Powrie, W. (1997), *Soil Mechanics: Concepts and Applications*, E & FN SPON, London.
11. Terzaghi, K. (1943), *Theoretical soil mechanics*, John Wiley and Sons Inc., New York.
12. Tomlinson, M. J. and Boorman, R. (1986), *Foundation design and construction*, Longman Scientific & Technical, New York.

(received on Feb. 23, 2006, accepted on Jun. 21, 2006)

Appendix

A.1 Calculation Parameters

ϕ'	γ	δ_w	D_f	L_w	B	A_b	A_s
26°	20kN/m^3	13°	0.37m	0.075m	0.025m	0.00188m^2	0.02775m^2

ϕ': Angle of shearing resistance; γ: Soil's unit weight; δ_w: Wall friction angle; D_f: Embedded length of wall, L_w: Longitudinal length of wall; B: Wall width; A_b: Area of cross-section of wall ($A_b=B\times L_w$); A_s: Area of wall sides ($A_s=2\times D_f\times L_w$)

A.2 Lower Bound Calculation for LB-01

(1) Calculation of P_{end}

From Fig. 10: $(\sigma_3')_A = 7.4kPa$,

$\frac{t_A}{s_A'} = \sin\phi' = \frac{\{s_A' - (\sigma_3')_A\}}{s_A'}$, therefore, $s_A' = \frac{(\sigma_3')_A}{(1-\sin\phi')}$

$s_A' = \frac{7.4}{(1-\sin 26°)} = 13.2kPa$

$\frac{s_B'}{s_A'} = \exp^{(2\Delta\theta\tan\phi')}$, where $\Delta\theta$=90°

$s_B' = 61.1kPa$

From Fig. 2 (a): $(\sigma_1')_B = s_B'(1+\sin\phi')$

$(\sigma_1')_B = 87.9kPa$

$P_{end} = (\sigma_1')_B \times A = 0.165kN = 16.5kg$

(2) Calculation of P_{side}

From Fig. 10: $\sigma_{3(low)}' = 7.1kPa$

$\frac{t_\delta}{s_{\delta(low)}'} = \sin\phi' = \frac{(s_{\delta(low)}' - \sigma_{3(low)}')}{s_{\delta(low)}'}$, therefore,

$s_{\delta(low)}' = \frac{\sigma_{3(low)}'}{(1-\sin\phi')}$

$s_{\delta(low)}' = \frac{7.1}{(1-\sin 26°)} = 12.6kPa$

$\frac{s_{\delta(high)}'}{s_{\delta(low)}'} = \exp^{(2\Delta\theta\tan\phi')}$, where $\Delta\theta$=22°

$s_{\delta(high)}' = 18.3kPa$

From Fig. 11: $t_{\delta(high)} = s_{\delta(high)}'\sin\phi'$

$t_{\delta(high)} = 8.02kPa$

$\tau_w = t_{\delta(high)}\sin 2\theta = 5.57kPa$, where q=22°

$P_{side} = \left\{\frac{1}{2}(\tau_w \times D_f)\right\}\times L_W \times 2 = \left\{\frac{1}{2}(5.57\times 0.37)\right\}\times 0.075\times 2$

$= 0.155kN = 15.5kg$

(3) Calculation of P_u

$P_u = P_{end} + P_{side} = 16.5 + 15.5 = 32kg$

A.3 Lower Bound Calculation for LB-02

(1) Calculation of Pside

From Fig. 13: $\sigma_v' = \gamma\times D_f = 20\times 0.37 = 7.4kPa$

(at wall tip level)

$\sigma_v' = s_A' + t_A\cos 2\theta$, therefore,

$s_A' = \sigma_v' - (s_A'\sin\phi'\cos 2\theta)$ where θ=9°

$s_A' = \frac{\sigma_v'}{(1+\sin\phi'\cos 2\theta)} = \frac{7.4}{(1+\sin 26°\cos 18°)} = 5.22kPa$

$\sigma_w' = s_A' - (\sigma_v' - s_A') = 5.22 - (7.4 - 5.22) = 3.04kPa$

$\tau_w = \sigma_w'\tan\delta_w = 3.04\times\tan 13° = 0.7kPa$

$P_{side} = \left\{\frac{1}{2}(\tau_w \times L_P)\right\}\times L_R \times 2$

$= \left\{\frac{1}{2}(0.7\times 0.37)\right\}\times 0.075\times 2 = 0.02kN = 2kg$

(2) Calculation of P_{end}

From Fig. 12: $(\sigma_1')_B = \gamma\times D_f = 20\times 0.37 = 7.4kPa$

(at wall tip level)

$\frac{s_B'}{s_A'} = \exp(2\Delta\theta\tan\phi')$, where $\Delta\theta$=189°

$s_B' = 130.6kPa$

From Fig. 2 (a): $(\sigma_1')_B = s_B'(1+\sin\phi')$

$(\sigma_1')_B = 187.85kPa$

$P_{end} = (\sigma_1')_B \times A = 0.352kN = 35.2kg$

(3) Calculation of P_u

$$P_u = P_{side} + P_{end} = 2 + 35.2 = 37.2kg$$

A.4 Upper Bound Calculation for PM-02

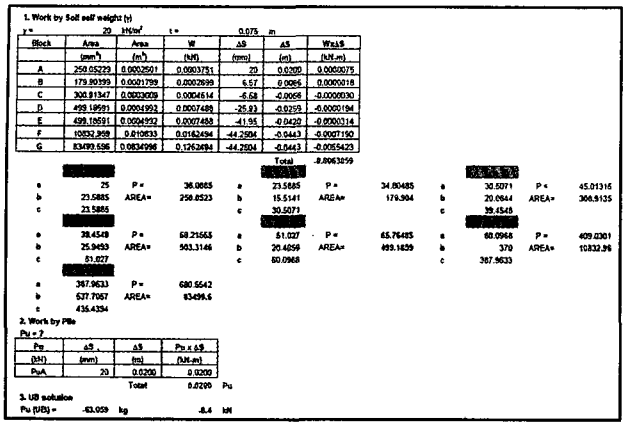

A.5 Conventional Calculation

The basis of the static or soil mechanics method of calculating the ultimate carrying capacity of a pile is that the ultimate carrying is equal to the sum of the ultimate resistance of the base of the pile and the ultimate skin friction over the embedded shaft length of the pile. This is expressed by the equation:

$$Q_u = Q_b + Q_s$$

where Q_b = base resistance; Q_s = shaft resistance.

Knowing the angle of shearing resistance of the soil at base level, Q_b can be calculated from Terzaghi's general equation.

In cohesionless soils:

$$Q_u = A_b \sigma_v' N_q + \overline{K}_s \overline{\sigma}_v \tan\delta_w A_s$$

where $\overline{\sigma}_v$ = average effective overburden pressure over embedded depth of pile, $N_q = e^{\pi \tan\phi'} \tan^2(45° + \frac{\phi'}{2})$, $\overline{K}_s = K_0 = 1 - \sin\phi'$.